



NRC Publications Archive Archives des publications du CNRC

Numerical modeling of electrowetting transport processes in digital microfluidics

Clime, L.; Brassard, D.; Veres, T.

This publication could be one of several versions: author's original, accepted manuscript or the publisher's version. / La version de cette publication peut être l'une des suivantes : la version prépublication de l'auteur, la version acceptée du manuscrit ou la version de l'éditeur.

For the publisher's version, please access the DOI link below. / Pour consulter la version de l'éditeur, utilisez le lien DOI ci-dessous.

Publisher's version / Version de l'éditeur:

<https://doi.org/10.1007/s10404-009-0491-9>

Microfluidics and Nanofluidics, 8, 5, pp. 599-608, 2010-05-01

NRC Publications Record / Notice d'Archives des publications de CNRC:

<https://nrc-publications.canada.ca/eng/view/object/?id=d82dbe03-0e4b-438d-9948-2f326fe1a61f>

<https://publications-cnrc.canada.ca/fra/voir/objet/?id=d82dbe03-0e4b-438d-9948-2f326fe1a61f>

Access and use of this website and the material on it are subject to the Terms and Conditions set forth at

<https://nrc-publications.canada.ca/eng/copyright>

READ THESE TERMS AND CONDITIONS CAREFULLY BEFORE USING THIS WEBSITE.

L'accès à ce site Web et l'utilisation de son contenu sont assujettis aux conditions présentées dans le site

<https://publications-cnrc.canada.ca/fra/droits>

LISEZ CES CONDITIONS ATTENTIVEMENT AVANT D'UTILISER CE SITE WEB.

Questions? Contact the NRC Publications Archive team at

PublicationsArchive-ArchivesPublications@nrc-cnrc.gc.ca. If you wish to email the authors directly, please see the first page of the publication for their contact information.

Vous avez des questions? Nous pouvons vous aider. Pour communiquer directement avec un auteur, consultez la première page de la revue dans laquelle son article a été publié afin de trouver ses coordonnées. Si vous n'arrivez pas à les repérer, communiquez avec nous à PublicationsArchive-ArchivesPublications@nrc-cnrc.gc.ca.



National Research
Council Canada

Conseil national de
recherches Canada

Canada

Numerical modeling of electrowetting transport processes for digital microfluidics

L. Clime · D. Brassard · T. Veres

Received: 18 June 2009 / Accepted: 28 July 2009 / Published online: 12 August 2009
© Springer-Verlag 2009

Abstract Electrical actuation and control of liquid droplets in Hele-Shaw cells have significant importance for microfluidics and lab-on-chip devices. Numerical modeling of complex physical phenomena like contact line dynamics, dynamic contact angles or contact angle hysteresis involved in these processes do challenge in a significant manner classical numerical approaches based on macroscopic Navier–Stokes partial differential equations. In this paper, we analyze the efficiency of a numerical lattice Boltzmann model to simulate basic transport operations of sub-millimeter liquid droplets in electrowetting actuated Hele-Shaw cells. We use a two-phase three-dimensional D3Q19 lattice Boltzmann scheme driven by a Shan–Chen-type mesoscopic potential in order to simulate the gas–liquid equilibrium state of a liquid droplet confined between two solid plates. The contact angles at the liquid–solid–gas interface are simulated by taking into consideration the interaction between fluid particles and solid nodes. The electrodes are designed as regions of tunable wettability on the bottom plate and the contact angles adjusted by changing the interaction strength of the liquid with these regions. The transport velocities obtained with this approach are compared to predictions from analytical models and very good agreement is obtained.

Keywords Lattice Boltzmann method · D3Q19 · Shan–Chen mesoscopic potential · Hele-Shaw cells · Electrowetting · Digital microfluidics

1 Introduction

Microfluidics is a very important field in the area of microelectromechanical systems (MEMS) (Kovas et al. 1998; Tanaka 2007) and lab-on-chip devices that is expanding very rapidly, stimulated by an impressive number of applications in biology, chemistry and medicine. Several issues related to the high pressures needed for pumping liquids through microchannels as well as the ineffective mixing at low Reynolds numbers (Ismagilov et al. 2001) combined with the inherent difficulties of designing scalable continuous-flow architectures severely limit the reliability and throughput of these devices in more complicated microfluidic architectures. A recent way to circumvent these difficulties is to implement architectures based on discrete droplets, the resulting devices being usually referred to as digital microfluidic microchips (Pollack et al. 2002). The liquid droplets are confined between two parallel plates [like in the Hele-Shaw cells (Hele-Shaw 1898)] and the basic operations such as transport, merging and splitting usually achieved by the electrowetting on dielectric (EWOD) effect (Beni and Hackwood 1981). This effect consists of a change in the solid–liquid contact angle due to an applied potential difference between the solid and the liquid. Since any change in the liquid–solid contact angle induced by the electrode voltage modifies locally the curvature of the liquid free surface (and so the internal pressure in the bulk liquid according to Laplace’s law), actuation forces toward regions of lower internal pressure can be achieved by using appropriate designs for the electrode system (Pollack et al. 2002). Usually the top electrode is a conductor connected to the ground (so the liquid droplets) whereas the bottom (activation) electrodes are covered with a thin dielectric layer. The microchips based on Hele-Shaw-like cells accompanied by a set of conducting electrodes able to move liquid droplets via

L. Clime (✉) · D. Brassard · T. Veres
NRC, Industrial Materials Institute, 75 Boul. de la Mortagne,
Boucherville J4B 6Y4, Canada
e-mail: Liviu.Clime@imi.cnrc-nrc.gc.ca

the EWOD effect are usually referred to as EWOD devices (Mugele and Baret 2005) and used as an alternative to classical continuous-flow microfluidics.

It is very difficult to accurately model the physical processes related to the motion of the contact line of the liquid droplets in EWOD devices. The main challenges are related to the dynamics of the liquid–gas interface, dynamic contact angle as well as the contact angle hysteresis (CAH). Since classical fluid dynamics methods (based on solving partial differential equations and a continuum description of the liquid) either leads to (1) stress singularities and multivalued velocity fields especially near the contact line (Sciffer 2000; Seppecher 1996) or (2) involve empirical relations with unknown parameters which can only be determined by fittings with experimental data (Sciffer 2000), alternative and promising numerical scheme based on discrete (atomistic) description of the liquid (molecular dynamics simulations) have been recently developed (He and Hadjiconstantinou 2003; Samsonov and Ratnikov 2007) but the necessary computational load for modeling real amounts of liquids in microfluidic devices is too large. One way to circumvent this difficulty and model larger systems while taking advantages from both continuum and discrete approaches is to use hybrid methods (Yasuda and Yamamoto 2008) obtained by coupling classical fluid computation schemes with molecular dynamics algorithms.

In the last years, the lattice Boltzmann method (LBM) (Chen and Doolen 1998; Succi et al. 1991) has experienced significant development due to the possibility to easily implement complex solid boundaries and multicomponent/multiphase systems in a unitary manner. The tremendous advantage of this relatively new approach is that it behaves like a classical Navier–Stokes solver in the bulk liquid whereas its mesoscopic nature becomes important at the interfaces (Zhang and Kwok 2004). Moreover, it allows for considering larger physical systems when compared to molecular dynamics methods and is able to capture all the physics from classical CFD approaches based on continuum representations. Thus, the LBM is a very appropriate numerical tool when interfacial phenomena and complex interactions with solid boundaries become important, as it is the case with the dynamics of liquid droplets in Hele–Shaw cells.

Several LBM schemes for simulating complex multiphase and multicomponent fluid flows are available in the literature. The first LBM-based multicomponent model has been developed by Gunstensen and Rothman (1993) and it was based on the lattice gas model of Rothman and Keller (1988). Phase separation and multiphase flows have successfully been simulated by using the method of Shan and

Chen (1993), Shan and Doolen (1995), based on the use of an interaction pseudopotential between different phases (or components). Free energy (Swift et al. 1995, 1996), mean-field (Zhang et al. 2004) or more consistent bottom-up (Melchionna and Marini Bettolo Marconi 2008) LBM approaches based on the thermodynamics of two-component fluids and the free-energy thermodynamic functional can also be used for modeling multiphase and interfacial dynamics.

In this paper, we evaluate the efficiency of a three-dimensional LBM scheme accompanied by a Shan–Chen interaction potential to model basic transport operations in EWOD devices. The actuation of the liquid droplets is performed by changing the interaction potential of the liquid with the electrodes and the separation between liquid and gas defined as an isosurface in the density scalar field. The numerical simulations are then compared to analytical models and good agreement is obtained.

2 LBM model

The LBM is a numerical version of the continuous (full) Boltzmann equation in which space, time and particle velocities are all discrete. The space (of one, two or three dimensions) is represented by a regular lattice with particles residing on the nodes and moving along a fixed (finite) number of directions. In this paper, we use a three-dimensional LBM scheme with 19 directions/velocities, well known in the literature as the D3Q19 scheme (Mei et al. 2000). The distributions of particles f_i on each direction $i = \overline{0, 18}$ (where 0 stands for particles at rest, 1–6 for the directions along lattice principal axes and 7–18 for the face diagonals) are iteratively updated according to the equation

$$f_i(\vec{x} + \vec{e}_i \Delta x, t + \Delta t) = f_i(\vec{x}, t) + \Omega_i[f(\vec{x}, t)] \quad (1)$$

where Δx and Δt are, respectively the space and time increments and $|\vec{e}_i| = \Delta x / \Delta t$. If the functional Ω_i is replaced by the BGK collision term (Bhatnagar et al. 1954) then Eq. 1 can be rewritten as

$$f_i(\vec{x} + \vec{e}_i, t + 1) = f_i(\vec{x}, t) - \frac{f_i - f_i^{\text{eq}}}{\tau}. \quad (2)$$

Here τ is the rate at which the local particle distributions relax to an equilibrium state and it is related to the kinematic viscosity of the fluid by

$$\nu = \frac{1}{3} \left(\tau - \frac{1}{2} \right). \quad (3)$$

The equilibrium distribution function can be written up to $O(u^2)$ as (Chen et al. 1992; Qian et al. 1992)

$$f_i^{\text{eq}} = \rho w_i \left[1 + 3\vec{e}_i \cdot \vec{u} + \frac{9}{2}(\vec{e}_i \cdot \vec{u})^2 - \frac{3}{2}u^2 \right] \quad (4)$$

where $w_i = 1/3$ if $i = 0$, $w_i = 1/18$ if $i = \overline{1, 6}$ and $w_i = 1/36$ if $i = \overline{7, 18}$. The quantities ρ and \vec{u} are two macroscopic variables related to the density and the local velocity of the fluid, respectively. They are computed at each iteration step via

$$\rho = \sum_{i=0}^{18} f_i \quad \text{and} \quad \vec{u} = \frac{1}{\rho} \sum_{i=0}^{18} f_i \vec{e}_i. \quad (5)$$

According to Shan and Chen (1993) and Shan and Doolen (1995), the coexistence of multiple phases at the nodes of the lattice can be simulated by shifting the velocities \vec{u} in Eq. 5 with the quantity

$$\Delta \vec{u} = \frac{\tau \vec{F}}{\rho} \quad (6)$$

where \vec{F} is an attractive short-range force of the form

$$\vec{F}(\vec{x}) = -G_{\text{LL}} \Psi(\vec{x}) \sum_i w_i \Psi(\vec{x} + \vec{e}_i) \quad (7)$$

and Ψ an interaction potential responsible for the equation of state (EOS) of the considered physical system. G_{LL} in the expression above is a negative quantity equivalent to a thermodynamic temperature and it is responsible for the liquid–gas density ratio as well as the surface tension coefficient. Several EOS can be incorporated into the above lattice Boltzmann scheme via the potential Ψ (Yuan and Schaefer 2006). As the physical processes related to digital fluidics and electrowetting analyzed in this paper are dominated by viscous and interfacial effects, the capillary number Ca defined as

$$Ca = \frac{\eta U}{\gamma} \quad (8)$$

can be chosen as a relevant dimensionless quantity. η in the equation above stands for the liquid viscosity, U for the liquid velocity and γ for the liquid surface tension coefficient. In order to reproduce the relevant Ca numbers in EWOD devices, we have selected an interaction potential that leads to one of the most numerically stable EOS (Shan and Chen 1994) that is

$$\Psi[\rho(\vec{x})] = \Psi_0 \exp\left(-\frac{\rho_0}{\rho(\vec{x})}\right), \quad (9)$$

where Ψ_0 and ρ_0 are two constant parameters responsible for the equilibrium values of liquid and gas densities after phase separation. By using this potential, liquid to gas density ratios of about 20 can easily be obtained before numerical instabilities caused by spurious velocities (Mei et al. 2000) start to appear. Although this density ratio is significantly lower than the water to air density ratio, we

will see in the following that the selected interaction potential can still be used to model accurately the displacement of liquid droplets in Hele-Shaw cells.

An example of EOS given by the pseudopotential in Eq. 9 is illustrated in Fig. 1a and the points corresponding to the phase separation at $G_{\text{LL}} = -120$, $\Psi_0 = 4$ and $\rho_0 = 200$ are highlighted. For this value of G_{LL} , a surface tension coefficient $\gamma^{\text{LB}} = 14.1$ is obtained by evaluating the variation of pressure across surfaces of spherical droplets of different radii (Fig. 1b) and applying the Laplace's law.

The wettability of solid obstacles (plates, electrodes, etc.) is modeled by assuming a default value for the interaction potential $\Psi(\vec{x})$ at all their nodes. The interaction constant in Eq. 7 is set to a specific value G_{LS} , the ratio $G_{\text{LL}}/G_{\text{LS}}$ being responsible for the contact angle at the contact line (CL) of the droplet. Moreover, bounce-back boundary conditions (Chen and Mei 1996) have been imposed at all these solid obstacle nodes. The interface between liquid and vapor states of densities ρ_l and ρ_g is

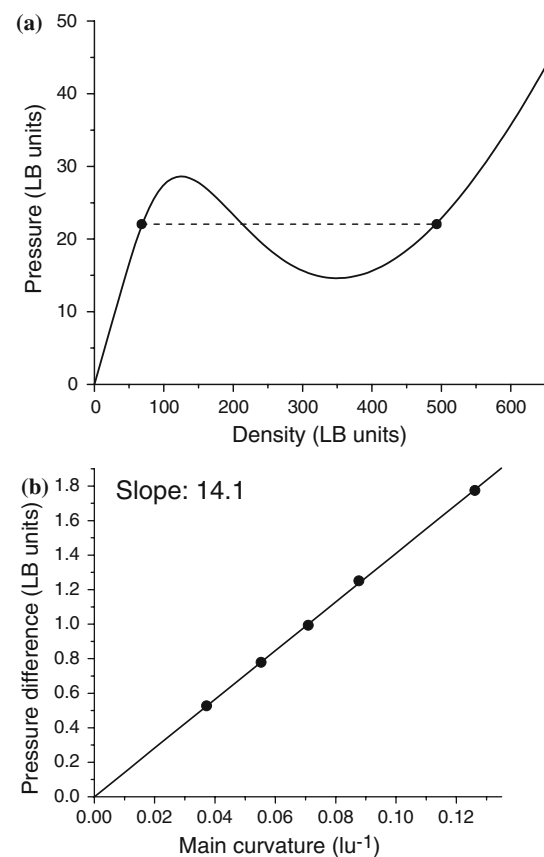


Fig. 1 **a** Equation of state (EOS) and equilibrium liquid–steam states (highlighted with *points*) obtained for $\Psi_0 = 4$, $\rho_0 = 200$ and $G_{\text{LL}} = -120$; **b** pressure difference due to the curvature of several simulated liquid spherical droplets (*points*) and linear fit with the Laplace's law (*full line*)

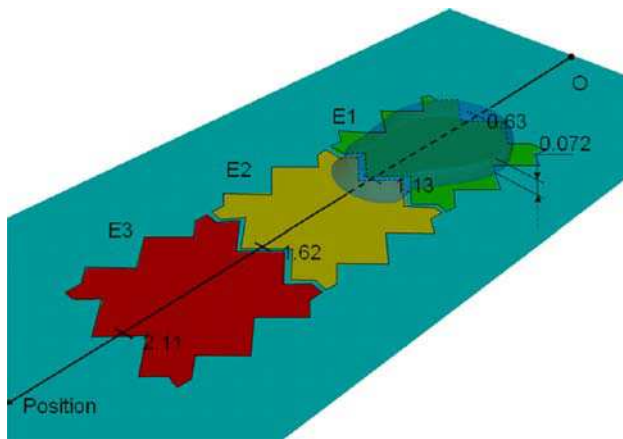


Fig. 2 3D representation of the EWOD device simulated by LBM: *bottom plate* containing three actuation electrodes (E1, E2 and E3) and a liquid droplet in a transport process from E1 to E2. The *top plate* is not shown in this figure and the numbers are all in mm. The dimensions of the simulation box in LB units (lu) are $608 \times 262 \times 18$

then represented by the isosurface $(\rho_l + \rho_g)/2$ in the mass density scalar field ρ given by Eq. 5. An example of such a representation is given in Fig. 2. The transition from lattice units to physical units employed in this figure is described in the next sections.

3 Analytical model

Lattice Boltzmann simulations are supposed to represent the physics of real systems so a correspondence between “lattice variables” [like lattice time units (ts) or lattice space units (lu)] and real physical units has to be found. To achieve this, the physical system is converted into a dimensionless one, by using a representative dimensionless parameter. The most challenging part of this parametrization procedure is to properly choose the dimensionless parameter. This is usually done by using analytical models describing simpler and representative processes for the problem under investigation (Sukop and Thorne 2005).

In the following, we describe an analytical model (Bahadur and Garimella 2006; Kumari et al. 2008) for the transport of liquid droplets in Hele-Shaw cells (Hele-Shaw 1898). According to this model, the motion of a cylindrical droplet of mass m and radius R between two parallel plates of spacing H is governed by (Kumari et al. 2008)

$$m \frac{d^2 x}{dt^2} = F_{\text{act}} - \frac{6\eta U}{H} 2\pi R^2 - \frac{1}{2} C \rho_g U^2 (2HR) - \zeta U (4\pi R) \quad (10)$$

where F_{act} is the actuation force (here induced by electrowetting effects), η the liquid dynamic viscosity, U the droplet transport velocity and ρ_g the gas mass density.

C and ζ are two phenomenological coefficients related to the drag of a cylinder in a viscous fluid flow and to the contact line friction force, respectively. If we neglect the inertial effects related to acceleration of the droplet as well as the drag force due to the filler gas and the friction at the contact line between the three phases (liquid–solid–gas), Eq. 10 becomes much simpler. At mechanical equilibrium, we thus have:

$$F_{\text{act}} = \frac{6\eta U}{H} 2\pi R^2 \quad (11)$$

that is the droplet motion is governed only by the equilibrium between the actuation force F_{act} and the viscous force due to the top and bottom plates. The next step in our parametrization analysis is to evaluate the actuation force in this equation. For a droplet at rest, the curvature has the same value at all points of the liquid–gas interface so there is no difference in the internal pressure between different parts of the droplet and consequently no actuation force will act upon the liquid droplet (Fig. 3a). If the contact angle in a specific region of the droplet is modified (Fig. 3b), the curvature of the interface changes accordingly and a pressure difference between this region and the rest of the droplet occurs. According to the fundamental principle of hydrostatics, a liquid always flows from regions of higher pressure toward regions of lower pressure, this being equivalent to the apparition of an actuation force F_{act} . Although the transition from this non-uniform and complex pressure field to an equivalent (and unique) actuation force is not

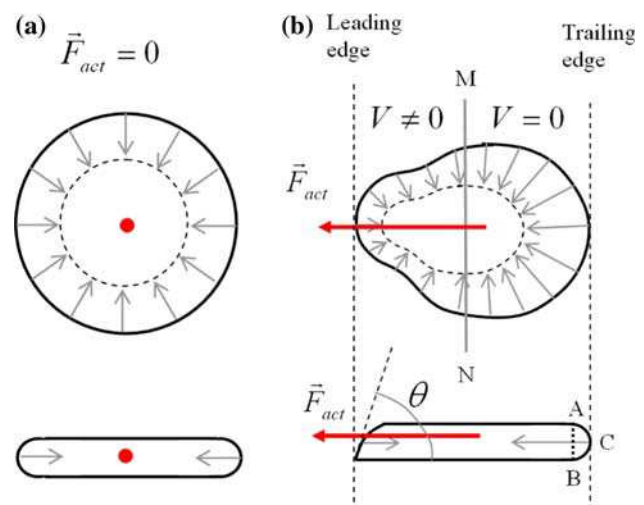


Fig. 3 Top and lateral views of the internal pressure effects and consequent actuation forces exerted by the liquid–gas interface at equilibrium (a) and when a change in the interface liquid–solid contact angle is induced by an applied potential (b). The force F_{act} is a consequence of changing the contact angle with the bottom plate in at the left side of MN

an easy task, we can obtain such equivalence by making some simplifying assumptions.

We consider that, in the absence of any applied potential on the electrodes, the out of plane curvature of the interface corresponds to a contact angle θ_{OFF} all along the liquid contact line. By applying a potential on the bottom plate (at the left side of MN—Fig. 3b), the contact angle θ_{OFF} is changed to θ_{ON} and an additional curvature $(\cos \theta_{\text{OFF}} + \cos \theta_{\text{ON}})/H$ is added to the initial in-plane curvature. According to the Laplace's law, the difference in internal pressure between the left and the right side of the droplet will be

$$\Delta p = \frac{\gamma}{H}(\cos \theta_{\text{ON}} - \cos \theta_{\text{OFF}}) \quad (12)$$

since the differences in internal pressure due to the in-plane curvature (R^{-1}) will cancel each other.

If we consider now that this pressure difference is uniformly distributed onto the droplet interface situated at the left side of MN, the force responsible for the droplet actuation in Eq. 11 can be written as

$$F_{\text{act}} = \int_{-\frac{\pi}{2}}^{+\frac{\pi}{2}} \Delta p R H \cos \alpha d\alpha = 2\Delta p R H. \quad (13)$$

We can replace now F_{act} in Eq. 11 by the expression above and obtain

$$U = \frac{\gamma H}{6\pi\eta R}(\cos \theta_{\text{ON}} - \cos \theta_{\text{OFF}}). \quad (14)$$

We thus obtain from Eq. 8

$$Ca = \frac{\eta U}{\gamma} = \frac{H}{6\pi R}(\cos \theta_{\text{ON}} - \cos \theta_{\text{OFF}}) \quad (15)$$

that is the capillary number Ca for the considered problem depends only on the geometry of the system (i.e., on the droplet aspect ratio H/R and its contact angles).

4 Parametrization of the LBM variables

From the analytical model presented in the previous section, it results that (1) the capillary number Ca can describe accurately the systems of interest if its geometry is known and (2) that the viscous drag and the interfacial tensions are the dominant forces in EWOD devices. Consequently, we decided to use the capillary number Ca as the characteristic dimensionless number for the parametrization of the LBM variables. In the following we use this number in order to pass from LBM units of length and time (lu and ts, respectively) to real units (m and s). From the definition of the capillary number Ca (Eq. 8) we can deduce that

$$Ca = \frac{\eta^R U^R}{\gamma^R} = \frac{\eta^{\text{LB}} U^{\text{LB}}}{\gamma^{\text{LB}}} \quad (16)$$

where indices “R” and “LB” stand respectively for the real and LBM systems. It results immediately that the two velocities weighted in m/s and lu/ts are given by

$$U^R = \left[\frac{\gamma^R}{\eta^R} Ca \right] \frac{\text{m}}{\text{s}} \quad \text{and} \quad U^{\text{LB}} = \left[\frac{\gamma^{\text{LB}}}{\eta^{\text{LB}}} Ca \right] \frac{\text{lu}}{\text{ts}}$$

where the square brackets denote the numerical (dimensionless) values of the corresponding quantities. From $U^R = U^{\text{LB}}$ we obtain

$$\left[\frac{\gamma^{\text{LB}}}{\eta^{\text{LB}}} \right] \frac{\text{lu}}{\text{ts}} = \left[\frac{\gamma^R}{\eta^R} \right] \frac{\text{m}}{\text{s}} \quad (17)$$

that is a relationship between the LBM units lu and ts. For water $\eta^R = 0.001 \text{ N s/m}^2$ and $\gamma^R = 0.0725 \text{ N/m}$ whereas the LBM algorithm described in Sect. 2 gives a dynamic viscosity $\eta^{\text{LB}} = 88.3$ and a surface tension coefficient $\gamma^{\text{LB}} = 14.1$ (both in LBM units). The dynamic viscosity η^{LB} is evaluated by using the numerical value of the density of the liquid phase as defined by Eq. 5. The relationship between velocity in LBM and real units is thus $1 \text{ lu/ts} = 454 \text{ m/s}$.

Although it is not necessary for an analysis of the droplet transport velocity, we decided for the sake of simplicity to also fix a relationship between the LBM and real length units. From now on, we consider that the diameter of a droplet, which is represented by 110 lu in the simulations, is of $500 \mu\text{m}$ (a typical value for real EWOD devices). A lattice unit thus corresponds to $1 \text{ lu} = 4.55 \mu\text{m}$. From Eq. 17 it results that the LBM unit time (ts) has to account about 10 ns (that is 100,000 LBM iteration steps correspond to 1 ms). The above values of $4.54 \mu\text{m}$ and 10 ns are used (Bahadur and Garimella 2006) all along the paper in order to pass from abstract lattice Boltzmann units (lu and ts) to real (physical) units of length and time, respectively.

5 Transport velocity

We want to address in this section the dependence of the transport velocity on the contact angle at the contact line of a liquid droplet actuated by electrowetting in a Hele-Shaw cell. A liquid droplet of about $500 \mu\text{m}$ diameter (110 lu) and $72 \mu\text{m}$ height (16 lu) is confined between two parallel plates (in Fig. 2 only the bottom plate, containing the actuation electrodes is shown). For this geometry, a numerical implementation of the algorithm on a supercomputer with Intel Itanium 2 microprocessors at 1.5 MHz is able to advance the droplet with 1 ms in about 100 CPUH (central processing unit, hours).

Several contact angles are first simulated by adjusting the solid–fluid interaction potential G_{LS} with respect to the fluid–fluid interaction strength (G_{LL}). The contact angle is then evaluated from the out-of-plane curvature radius R of the liquid–gas interface (Fig. 4a) by using the surface generated by the rotation of the arc BB' around the droplet symmetry axis (the regions AB and $B'A'$ are eliminated from this analysis in order to avoid any influence of the solid obstacle density on the evaluated contact angles). As shown in Fig. 4b, a full range of contact angles from 0 to 180° can be simulated for $G_{LL} = -120$ and $G_{LS} \in [-300, -50]$, respectively. A value of the contact angle of 0° corresponds to a value of G_{LS} of about -300 whereas a complete wettability of the surface, that is a nearly 0° contact angles can be obtained for $G_{LS} \cong -50$. As already pointed out in the literature (Zhang et al. 2004), the dependence of the contact angle on the liquid–solid interaction strength G_{LS} is almost linear (Fig. 4b). However, a better fit for our simulations can be obtained with $\theta(|G_{LS}|) = 198^\circ - 0.37|G_{LS}| - 8 \times 10^{-4}|G_{LS}|^2$, that is a second degree polynomial. By using this dependence, the

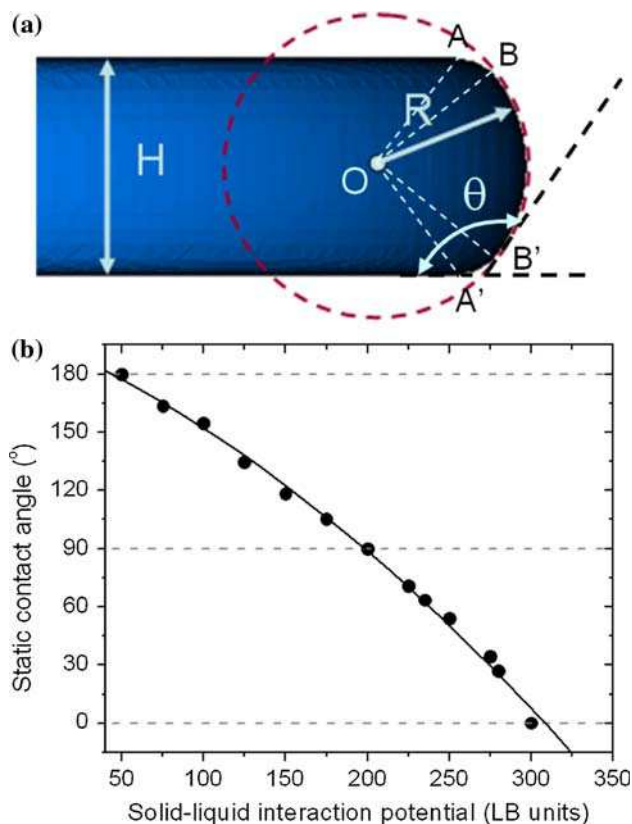


Fig. 4 **a** Lateral view of a simulated liquid droplet at $G_{LS} = -125$ that corresponds to a static contact angle of about $\theta = 135^\circ$; **b** simulated contact angles between 0° and 180° obtained by adjusting the potential of the electrodes between 300 and 50 (LB units), respectively. The interpolation curve corresponds to the function $\theta(|G_{LS}|) = 198^\circ - 0.37|G_{LS}| - 8 \times 10^{-4}|G_{LS}|^2$.

value of G_{LS} corresponding to a desired contact angle at the liquid–solid interface can easily be found. It is also possible to link the interaction strength parameter G_{LS} to the electric potential used for the activation of the electrodes if the electric potential dependence of the contact angle at these electrodes is known. One example of such an experimental dependence can be found in (Brassard et al. 2008). At relatively small values of the applied voltage (before the contact angle saturation) a simple quadratic dependence of the contact angle with the applied voltage $\cos(\theta) \propto U^2$ can be employed (Li and Fang 2009).

The numerical algorithm presented in Sect. 2 is applied to the nodes of a regular lattice of dimensions $608 \times 262 \times 18$ (each of them in lattice units, lu). The largest dimension corresponds to the direction of motion of the droplet (indicated by the position arrow in Fig. 2), whereas the smallest one represents the distance between the two plates of the cell. By using the results of the parametrization in Sect. 4, this simulation box will correspond to a real cell of dimensions $2.736 \text{ mm} \times 1.179 \text{ mm} \times 0.072 \text{ mm}$ (two lattice points are always subtracted on the O_z directions since they correspond to the bottom and top plates). On the bottom plate, three interdigitated comb-shaped electrodes labeled as E1, E2 and E3 (Fig. 2) are designed as regions of tunable interaction potential (the size of each electrode being of about 110 lu, that is approximately 0.5 mm). We considered in our simulations this comb-shaped geometry of the electrodes since it is largely used in the design of EWOD devices (Brassard et al. 2008) so comparisons to experimental data already available in the literature would be easier and more appropriate than having simple rectangular electrodes. These regions can be activated or deactivated by setting different potentials G_{LS} at different times (iterations) of the simulation. The top plate (not shown in Fig. 2) is homogeneous in the sense that we set the same value of the interaction constant G_{LS} at all its points. In the following we will refer to the value of G_{LS} on the inactive plates or electrodes as the “OFF” values. The values of G_{LS} applied on electrodes in order to actuate the droplet will be referred to as “ON” interaction constant values.

Each simulation starts with a cylindrical droplet above the electrode E1 and a thermalization period of about 10,000 iterations. During this period, densities inside and outside the liquid droplet as well as contact angles at the solid–liquid–gas interfaces reach their equilibrium values according to the considered EOS (see Fig. 1a) and the “OFF” interaction constant G_{LS} , respectively. At the end of this thermalization period, the interaction constant G_{LS} at the electrode E2 is changed to ON such that the contact angle above this electrode is changed and a difference in the internal pressure of the droplet generated. In our numerical simulation for example, we set the OFF interaction potential of the plates to $G_{LS} = -190$, which

corresponds to a contact angle slightly above but not too far from 90° . The activation of a specific electrode is made by setting the ON interaction potentials to $G_{LS} \in \{-225, -250, -260, -275, -300\}$ which correspond to contact angles of $72^\circ, 54^\circ, 41^\circ, 35^\circ$ and 0° , respectively. A top view of the droplet motion when the electrodes E2 and E3 are successively activated with $G_{LS} = -275$ is shown in Fig. 5. The time dependence of the position of leading and trailing edges as well as the length of the droplet are shown in Fig. 6. The transport process begins with a nucleation period in which the contact angle at the electrode E2 changes at the tips of the imbedded dents. The liquid then begins to move slightly toward this electrode. As the liquid invades E2, the droplet elongates such that the leading edge moves faster than the trailing one. When the liquid approaches the extremity of the electrode E2, the leading edge slows down and an increase in the velocity of trailing edge is observed. The liquid droplet finally stops when it

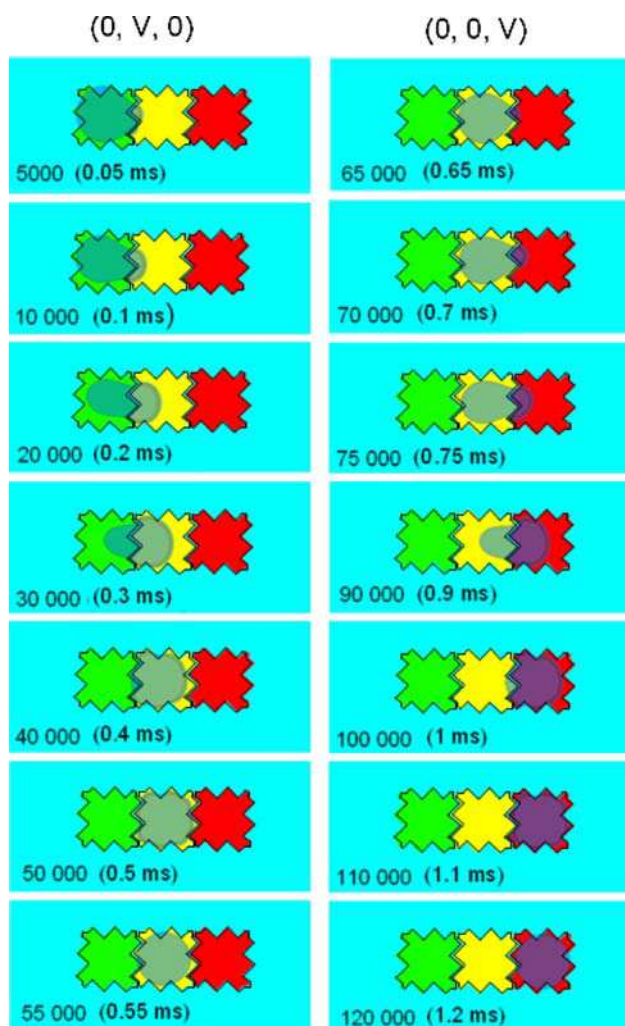


Fig. 5 Top view of a two-step transport process of a liquid droplet by using three electrodes and $G_{LS} = -275$ (the movie is also available as supplementary information)

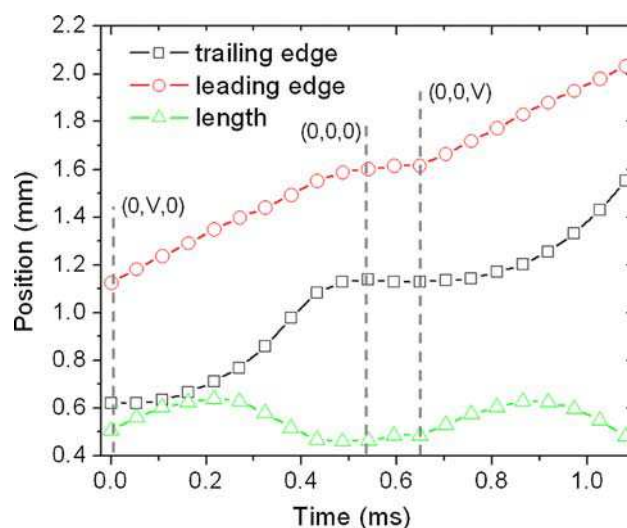


Fig. 6 Time dependence of leading (circles) and trailing (squares) edges as well as the length (triangles) of the droplet

touches the boundary between E2 and E3 and reacquires its initial equilibrium shape after E2 is completely deactivated. A similar transport process is obtained by activating E3 at the same value of the interaction potential $G_{LS} = -275$ while maintaining E2 deactivated (right column in Fig. 5).

In an attempt to understand applicability and limitations of both numerical and analytical models, the average velocities obtained at afore mentioned activation potentials (contact angles) are compared with predictions from the analytical model Eq. 11. As seen in Fig. 7, the agreement is very good even if we have neglected the last two terms in Eq. 10 related to the viscous drag from the gas and the contact line droplet friction. It is noteworthy that the slight difference observed between lattice Boltzmann and analytical results (especially at lower values of the contact angle) does not originate from the approximation we made by removing the last two terms of in Eq. 10. Indeed, the effect of these terms would be to further reduce the analytical velocity of the droplet (full line in Fig. 7) and so to increase the discrepancy between numerical and analytical approaches. The observed difference could rather originate from the higher deformation of the droplet at high transport velocities. We indeed observed that, as the transport velocity is increased, the longitudinal dimension of the droplet increases at the expense of its transversal one thus decreasing the effective hydrodynamic radius. Variations of the transport velocity in the range of the observed discrepancies in Fig. 7 can easily be obtained by modifying the radius of the droplet in Eq. 14 by about 9%, which is very plausible when compared to droplet shapes in Fig. 5 and time dependence of the droplet length in Fig. 6. Thus, we conclude that despite the low density ratios usually obtained in multiphase lattice Boltzmann simulations, the

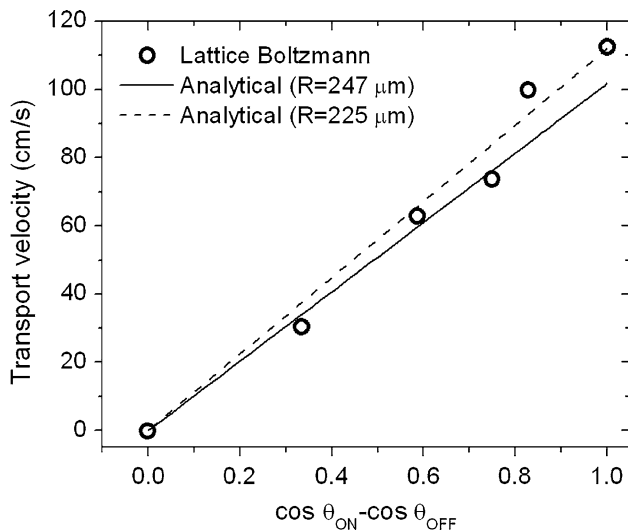


Fig. 7 Numerical (circles) and analytical (lines) contact angle dependence of the average transport velocity

gaseous phase does not significantly affect the motion of droplets in EWOD simulations. Good agreement with simple analytical predictions can also be obtained as long as the shape of the droplet is not deformed too strongly by the electrowetting pulling force.

To compare our simulation results with the values obtained in real EWOD devices, we should first note that real devices typically operate with rather small differences between ON and OFF contact angles (Brassard et al. 2008) compared to the simulations we showed previously. For example, a pair of contact angles often employed in real EWOD devices is 110° for the OFF state (inactive regions on the plates) and 80° for the active electrodes (ON states). As shown in Fig. 8, we thus made simulations of transport processes with these values of the contact angles. We found an average velocities of about 40 cm/s, which is at least 2–3 times larger than experimental velocities achieved in similar real EWOD devices (Brassard et al. 2008). We believe this discrepancy between the LBM simulations and the velocities values obtained in real EWOD devices is due to CAH (that was not considered in the simulations). Indeed, when the difference is rather small between ON and OFF contact angles (as is the case with real EWOD devices), the transport velocities are very sensitive to small variations of the contact angles (due to the CAH effect, for example). As we can see in Fig. 8b, when $\cos \theta_{\text{ON}} - \cos \theta_{\text{OFF}}$ is smaller than 0.1, variations of the contact angles of only few degrees can be responsible for relative variations of the transport velocities up to 100%. One should also note that this plot has been obtained by accounting the influence of only the advancing contact angle on the activated electrode (E2). If we take into account the effect of CAH on all four contact angles (advancing and receding on both plates) the

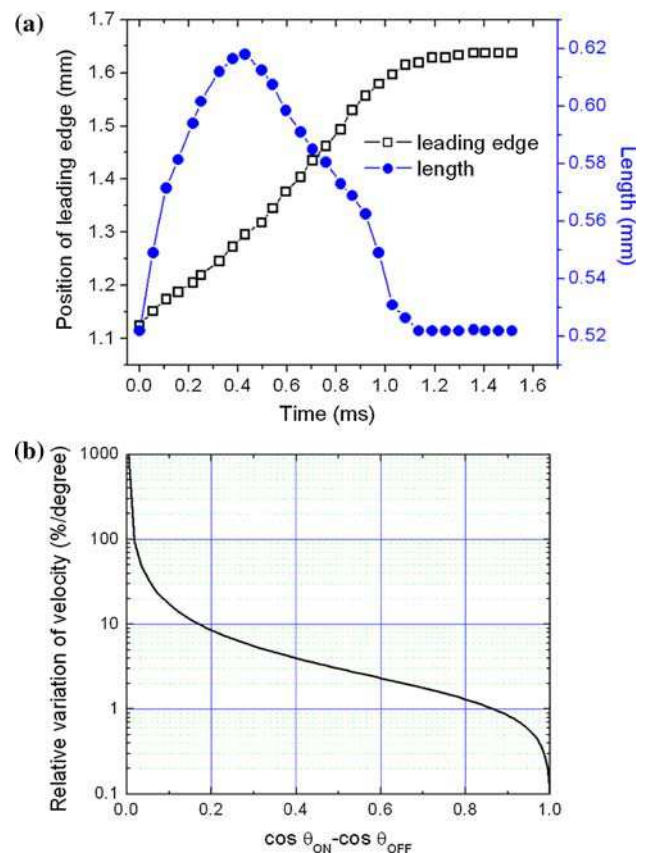


Fig. 8 **a** Time dependence of the leading edge position and the length of the droplet for $\theta_{\text{OFF}} = 110^\circ$ and $\theta_{\text{ON}} = 80^\circ$ applied on E2; **b** contact angle dependence of the relative variation of the droplet transport velocity

variation of the transport velocity could easily reach 200–300%, thus explaining the observed difference. This means in our view that the wetting phenomena in real EWOD devices are affected by hysteresis that is the advancing and receding contact angles of the droplet can be substantially different from the measured static values. These variations of the contact angles due to the CAH should thus be introduced into the LBM in order to correctly describe the transport processes at these low velocity regimes. This is a very challenging issue for numerical models since the static hysteresis is related to microscopic imperfections of the solid surfaces (Ramos-Canut 2005) that are difficult to address by LBM, mainly due to the mesoscopic (and not microscopic) nature of these approaches. This difficulty may be addressed by either refining the mesh (Filipova and Hanel 1998) near nanostructured surfaces or phenomenologically introducing irreversible and velocity dependent components to the interaction force with solid obstacles. In the present approach, this effect could also be taken into consideration by simply modifying the advancing and receding contact angles according to the observed CAH at the considered solid surfaces.

6 Concluding remarks

LBM is a powerful numerical technique able to model complex processes related to digital fluidics in Hele-Shaw cells. The mesoscopic nature of this method coupled with its ability to model multiphase flows offer tremendous advantages over other traditional techniques. Since viscous and interfacial effects are the most relevant forces for the transport of sub-micrometric droplets in EWOD devices, the capillary number Ca can be used in order to relate lattice Boltzmann units to real (SI) physical units. The Ca number can further be related to the electrowetting number by relating the LB liquid–solid interaction potential constant (G_{LS}) to the real electric voltage via the static liquid–solid contact angle.

The low density ratios usually obtained in LBM simulations are not an issue in modeling processes related to digital fluidics. The influence of the gas phase on the transport velocity of sub-micrometric liquid droplets is found to be insignificant even at values of about 20 for these ratios. Our LBM simulations show that maximal velocities experimentally obtained in real EWOD devices are still very low, the effect being at only 10% of its maximal achievable transport velocity. At these regimes, variations of few degrees only in the contact angles due to surface imperfections (like CAH effects) can have a drastic influence on the transport velocity, thus making the comparisons of LBM simulations to experiments very challenging. The influence of the CAH on the transport velocity is drastically reduced at higher differences between ON and OFF contact angles. For example, when the difference $\cos \theta_{ON} - \cos \theta_{OFF}$ related to the ON and OFF contact angles is about 0.5, a relative variation of the transport velocity of about only few percents by degree is obtained. However, since these contact angles are not achievable yet in experimental devices, further LBM approaches to the modeling of EWOD basic operations need to include the effects related to imperfections on solid surfaces.

Acknowledgments Computational resources were provided by the Réseau québécois de calcul de haute performance (RQCHP).

References

- Bahadur V, Garimella SV (2006) An energy-based model for electrowetting-induced droplet actuation. *J Micromech Microeng* 16:1494
- Beni G, Hackwood S (1981) Electro-wetting displays. *App Phys Lett* 38:207
- Bhatnagar PL, Gross EP and Krook M (1954) A model for collision processes in gases. I: small amplitude processes in charged and neutral one-component system. *Phys Rev* 94:511
- Brassard D, Malic L, Normandin F, Tabrizian M, Veres T (2008) Water-coil core-shell droplets for electrowetting-based digital microfluidic devices. *Lab Chip* 8:1342
- Chen S, Doolen GD (1998) Lattice Boltzmann method for fluid flows. *Annu Rev Fluid Mech* 30:329
- Chen S, Mei R (1996) On boundary conditions in lattice Boltzmann method. *Phys Fluids* 8:2527
- Chen H, Chen S, Matthaeus WH (1992) Recovery of the Navier–Stokes equations using a lattice-gas Boltzmann method. *Phys Rev A* 45:R5339
- Filipova O, Hanel D (1998) Grid refinement for lattice-BGK models. *J Comput Phys* 147:219
- Gunstensen AK, Rothman DH (1993) Lattice Boltzmann studies of immiscible two phase flow through porous media. *J Geophys Res* 98:6431
- He G, Hadjiconstantinou NG (2003) A molecular view of Tanner’s law: molecular dynamics simulations of droplet spreading. *J Fluid Mech* 497:123
- Hele-Shaw HS (1898) The flow of water. *Nature* 58:34
- Ismagilov RF, Ng JMK, Paul JA, Kenis PJA, George M, Whitesides GM (2001) Microfluidic arrays of fluid–fluid diffusional contacts as detection elements and combinatorial tools. *Anal Chem* 73:5207
- Kovas GTA, Maluf NI, Petersen KE (1998) Bulk micromachining of silicon. *Proc IEEE* 86:1536
- Kumari N, Bahadur V, Garimella SV (2008) Electrical actuation of dielectric droplets. *J Micromech Microeng* 18:085018
- Li H, Fang H (2009) Lattice Boltzmann simulation of electrowetting. *Eur Phys J Special Topics* 171:129
- Mei R, Shyy W, Yu D, Luo L-S (2000) Lattice Boltzmann method for 3-D flows with curved boundaries. *J Comput Phys* 161:680
- Melchionna S, Marini Bettolo Marconi U (2008) Lattice Boltzmann method for inhomogeneous fluids. *Europhys Lett* 81:34001
- Mugele F, Baret J-C (2005) Electrowetting: from basics to applications. *J Phys Condens Matter* 17:R705
- Pollack MG, Shenderov AD, Fair RB (2002) Electrowetting-based actuation of droplets for integrated microfluidics. *Lab Chip* 2:96
- Qian YH, d’Humi re D, Lallemand P (1992) Lattice BGK models for Navier–Stokes equations. *Europhys Lett* 17:479
- Ramos-Canut S (2005) Wetting properties of nanostructured surfaces Nuclear Instruments and Methods in Physics Research Section B: Beam Interactions with Materials and Atoms 245:322
- Rothman DH, Keller JM (1988) Immiscible cellular-automaton fluids. *J Stat Phys* 52:1119
- Samsonov VM, Ratnikov AS (2007) Comparative molecular dynamics study of simple and polymer nanodroplet spreading. *Colloids Surfaces A Physicochem Eng Asp* 298:52
- Sciffier S (2000) A phenomenological model of dynamic contact angle. *Chem Eng Sci* 55:5933
- Sepp cher P (1996) Moving contact angles in the Cahn–Hilliard Theory Int. *J Eng Sci* 34:977
- Shan X, Chen H (1993) Lattice Boltzmann model for simulating flows with multiple phases and components. *Phys Rev E* 47:1815
- Shan X, Chen H (1994) Simulation of nonideal gases and liquid–gas phase transitions by the lattice Boltzmann equation. *Phys Rev E* 49:2941
- Shan X, Doolen GD (1995) Multicomponent lattice-Boltzmann model with interparticle interaction. *J Stat Phys* 81:379
- Succi S, Benzi R, Higuera F (1991) The lattice-Boltzmann equation—a new tool for computational fluid dynamics. *Phys D* 47:219
- Sukop MC, Thorne DT (2005) Lattice Boltzmann modeling—an introduction to geoscientists and engineers. Springer, Berlin
- Swift MR, Osborn WR, Yeomans JM (1995) Lattice Boltzmann simulation of nonideal fluids. *Phys Rev Lett* 75:830
- Swift MR, Orlandini SE, Osborn WR, Yeomans JM (1996) Lattice Boltzmann simulations of liquid–gas and binary-fluid systems. *Phys Rev E* 54:5041

- Tanaka M (2007) An industrial and applied review of new MEMS devices features. *Microelectron Eng* 84:1341
- Yasuda S, Yamamoto R (2008) A model for hybrid simulations of molecular dynamics and computational fluid dynamics. *Phys Fluids* 20:113101
- Yuan P, Schaefer L (2006) Equations of state in lattice Boltzmann model. *Phys Fluids* 18:042101
- Zhang J, Kwok DY (2004) Lattice Boltzmann Study on the contact angle and contact line dynamics of liquid-vapor interface. *Langmuir* 20:8137
- Zhang J, Baoming L, Kwok DY (2004) Mean-field free-energy approach to the lattice Boltzmann method for liquid–vapor and solid–fluid interfaces. *Phys Rev E* 69:032602